**Astronomy & Astrophysics**

# Chemistry of $C_3$ and carbon chain molecules in DR21(OH)[*]

B. Mookerjea[1], G. E. Hassel[2], M. Gerin[3], T. Giesen[4], J. Stutzki[4], E. Herbst[5], J. H. Black[6], P. F. Goldsmith[7], K. M. Menten[8], J. Krełowski[9], M. De Luca[3], T. Csengeri[8], C. Joblin[10,11], M. Kaźmierczak[12], M. Schmidt[13] J. R. Goicoechea[14], and J. Cernicharo[14]

[1] Tata Institute of Fundamental Research, Homi Bhabha Road, 400005 Mumbai, India
    e-mail: bhaswati@tifr.res.in
[2] Department of Physics and Astronomy, Siena College, Loudonville, NY 12211, USA
[3] LERMA, CNRS, Observatoire de Paris and ENS, France
[4] I. Physikalisches Institut, University of Cologne, Germany
[5] Department of Chemistry, University of Virginia, Charlottesville, VA 22904 USA
[6] Onsala Space Observatory, Chalmers University of Technology, 43992 Onsala, Sweden
[7] JPL, California Institute of Technology, Pasadena, USA
[8] MPI für Radioastronomie, Bonn, Germany
[9] Nicolaus Copernicus University, Toruń, Poland
[10] Université de Toulouse, UPS-OMP, IRAP, Toulouse, France
[11] CNRS, IRAP, 9 Av. colonel Roche, BP 44346, 31028 Toulouse Cedex 4, France
[12] SRON Netherlands Institute for Space Research, Landleven 12, 9747 AD Groningen, The Netherlands
[13] Nicolaus Copernicus Astronomical Center (CMAK), Toruń, Poland
[14] Centro de Astrobiología, CSIC-INTA, 28850 Madrid, Spain

**ABSTRACT**

*Context.* $C_3$ is the smallest pure carbon chain detected in the dense environment of star-forming regions, although diatomic $C_2$ is detected in diffuse clouds. Measurement of the abundance of $C_3$ and the chemistry of its formation in dense star-forming regions has remained relatively unexplored.
*Aims.* We aim to identify the primary $C_3$ formation routes in dense star-forming regions following a chemical network producing species like CCH and $c$-$C_3H_2$ in the star-forming cores associated with DR21(OH), a high-mass star-forming region.
*Methods.* We observed velocity resolved spectra of four ro-vibrational far-infrared transitions of $C_3$ between the vibrational ground state and the low-energy $\nu_2$ bending mode at frequencies between 1654–1897 GHz using HIFI on board *Herschel*, in DR21(OH). Several transitions of CCH and $c$-$C_3H_2$ were also observed with HIFI and the IRAM 30 m telescope. Rotational temperatures and column densities for all chemical species were estimated. A gas and grain warm-up model was used to obtain estimates of densities and temperatures of the envelope. The chemical network in the model was used to identify the primary $C_3$ forming reactions in DR21(OH).
*Results.* We detected $C_3$ in absorption in four far-infrared transitions, $P(4)$, $P(10)$, $Q(2)$, and $Q(4)$. The continuum sources MM1 and MM2 in DR21(OH), though spatially unresolved, are sufficiently separated in velocity to be identified in the $C_3$ spectra. All $C_3$ transitions are detected from the embedded source MM2 and the surrounding envelope, whereas only $Q(4)$ and $P(4)$ are detected toward the hot core MM1. The abundance of $C_3$ in the envelope and MM2 is $\sim 6 \times 10^{-10}$ and $\sim 3 \times 10^{-9}$, respectively. For CCH and $c$-$C_3H_2$, we only detect emission from the envelope and MM1. The observed CCH, $C_3$ and $c$-$C_3H_2$ abundances are most consistent with a chemical model with $n_{H_2} \sim 5 \times 10^6$ cm$^{-3}$, a post-warm-up dust temperature $T_{max} = 30$ K, and a time of $\sim 0.7$–3 Myr.
*Conclusions.* Post-warm-up gas phase chemistry of $CH_4$ released from the grain at $t \sim 0.2$ Myr and lasting for 1 Myr can explain the observed $C_3$ abundance in the envelope of DR21(OH), and no mechanism involving photodestruction of PAH molecules is required. The chemistry in the envelope is similar to the warm carbon chain chemistry found in lukewarm corinos. We interpret the observed lower $C_3$ abundance in MM1 as compared to MM2 and the envelope to be due to the destruction of $C_3$ in the more evolved MM1. The timescale for the chemistry derived for the envelope is consistent with the dynamical timescale of 2 Myr derived for DR21(OH) in other studies.

**Key words.** ISM: molecules – ISM: lines and bands – ISM: individual objects: DR21(OH) – astrochemistry – radiative transfer – molecular data

## 1. Introduction

Small carbon chains are important for the chemistry of stellar and interstellar environments for several reasons: they are ubiquitous throughout the interstellar medium (Ádámkovics et al. 2003), they are likely to participate in the formation of

long carbon chain molecules, and they are products of photofragmentation cascades of polycyclic aromatic hydrocarbons (PAHs; Radi et al. 1988; Pety et al. 2005). Triatomic carbon, $C_3$, was first tentatively identified in interstellar gas by Van Orden et al. (1995) and Haffner & Meyer (1995). The mid-infrared spectrum of $C_3$ ($\nu_3$ antisymmetric stretching mode) was measured in the circumstellar envelope of CW Leo (IRC +10216) by Hinkle et al. (1988), and in low-resolution interstellar absorption in the far-IR ($\nu_2$ bending mode) toward the Sgr B2 star-forming

---

**Table 1.** Properties of the sources in DR21(OH).

| Component | $\alpha$(2000) | $\beta$(2000) | $v_{LSR}$ (km s$^{-1}$) | Mass$^a$ ($M_\odot$) | $T_d$ | $N(H_2)^b$ ($10^{23}$cm$^{-2}$) | $\langle n(H_2)\rangle$ ($10^7$ cm$^{-3}$) | References |
|---|---|---|---|---|---|---|---|---|
| MM1 | $20^h39^m01^s.0$ | $42°22'48''$ | $-4.1 \pm 0.3$ | 88 | 58 | 4.5 | 4.1 | 1, 2 |
| MM2 | $20^h39^m00^s.4$ | $42°22'43''.8$ | $-0.7 \pm 0.3$ | 143 | 30 | 7.4 | 6.8 | 1, 2 |
| Envelope | ... | ... | $-3.1 \pm 0.3$ | 118$^c$ | | 3.5 | 0.3 | 1, 3, 4 |

**Notes.** $^{(a)}$ All estimated for a distance of 1.5 kpc. $^{(b)}$ Within a 15″ beam. $^{(c)}$ Mass of the envelope derived by removing the contributions of MM1 and MM2 from the total mass of the region estimated by Motte et al. (2007).

**References.** (1) Mangum et al. (1991); (2) Mangum et al. (1992); (3) Wilson & Mauersberger (1990); (4) Motte et al. (2007).

region and IRC+10216 by Cernicharo et al. (2000). Giesen et al. (2001) discussed new laboratory data on the vibrational spectrum of $C_3$ in its low-frequency bending mode and revisited the first identification of the $\nu_2$ $R(2)$ line in absorption toward Sgr B2 (Van Orden et al. 1995). The abundance and excitation of $C_3$ with a large range of rotational temperatures in translucent clouds have also been determined convincingly (Maier et al. 2001; Roueff et al. 2002; Oka et al. 2003; Ádámkovics et al. 2003) through observations at optical wavelengths. In addition, Galazutdinov et al. (2002) demonstrated that the $C_3$ abundance is related neither to interstellar reddening nor to the intensities of diffuse interstellar bands.

DR21(OH) lies 2′ north of the H II region DR21, in the Cygnus X H II complex. The distance to DR21(OH) has recently been accurately determined by trigonometric parallax measurements of its associated methanol masers as $1.50^{+0.08}_{-0.07}$ kpc (Rygl et al. 2012). Interferometric and high-resolution single-dish observations both in continuum and molecular lines have shown multiple peaks in DR21(OH) (Wilson & Mauersberger 1990; Mangum et al. 1991, 1992; Chandler et al. 1993). Mangum et al. (1992) resolved the main DR21(OH) peak into two sources, MM1 and MM2, and MM2 into two subsources, MM2-A and MM2-B. Synthesis imaging of $NH_3$ emission from the region has clearly resolved MM1 and MM2, which have radial velocities $-4.1 \pm 0.3$ km s$^{-1}$ and $-0.7 \pm 0.3$ km s$^{-1}$, respectively (Mangum et al. 1992). Both star-forming cores MM1 and MM2 in DR21(OH) are young, with no visible H II region and only very weak continuum emission at the centimeter wavelengths (Argon et al. 2000). Dust continuum observations suggest that MM1 is the brighter source ($L = 1.7 \times 10^4$ $L_\odot$; ZAMS B0V star) and shows evidence of star formation, whereas MM2 ($L = 1.2 \times 10^3$ $L_\odot$; early B star), though more massive, is fainter and most likely at an earlier stage of evolution. The region is characterized as a high-mass star-forming region due to the detection of centimeter and millimeter maser emission from numerous transitions, e.g., $H_2O$, OH and $CH_3OH$ (Araya et al. 2009; Fish et al. 2005; Mangum et al. 1992; Plambeck & Menten 1990). MM1 also contains ground-state OH masers at 1.6 GHz and 6.7 GHz class II $CH_3OH$ masers near the peak of the dust and centimeter continuum emission (Argon et al. 2000; Fish et al. 2005; Rygl et al. 2012). In a recent interferometric study of the continuum emission at 1.4 mm from DR21(OH), Zapata et al. (2012) have resolved MM1 and MM2 into nine compact sources. Five of the compact sources are associated with MM1 and four with MM2. Two of the compact sources associated with MM1 (SMA6 and SMA7) seem to show hot core activity. White et al. (2010) have observed multiple transitions of CO from 4–3 to 13–12 using *Herschel*/SPIRE to conclude the presence of two components at 80 K and 180 K from a rotation temperature analysis. From an LVG analysis, these authors obtain $T_{kin} = 125$ K

and $n_{H_2} = 7 \times 10^4$ cm$^{-3}$. We summarize selected properties of all emission components in DR21(OH) as available from the literature in Table 1. All values in Table 1 correspond to a distance of 1.5 kpc.

With its broad frequency coverage, high sensitivity, and spectral resolution, the Heterodyne Instrument for the Far-Infrared (HIFI; de Graauw et al. 2010) on board the *Herschel* Space Observatory (Pilbratt et al. 2010), has provided for the first time the opportunity for a systematic study of carbon chain molecules such as $C_3$ through probing several ro-vibrational lines at full spectral resolution. The results presented here are a part of the PRISMAS "PRobing InterStellar Molecules with Absorption line Studies" key program (Gerin et al. 2010).

The primary aim of the paper is to understand the $C_3$ formation mechanism. Observations of diffuse interstellar gas at optical and IR wavelengths have shown a strong correlation between the column densities of $C_3$ and $C_2$. This suggests that $C_3$ and $C_2$ are in the same chain of chemical reactions (Oka et al. 2003). The formation routes for $C_3$ starting from $C_2$ also involved the production of CCH and $c$-$C_3H_2$. However, no transitions of $C_2$ are available at longer wavelengths (far-infrared and longer), which can be used to detect $C_2$ in dense star-forming regions, where $C_3$ is detected in absorption (Mookerjea et al. 2010). Thus, to understand the formation pathway of $C_3$, we compare the abundances of $C_3$, CCH, and $c$-$C_3H_2$, with results of chemical models of dense star-forming cores.

## 2. Observations

### 2.1. Herschel data: $C_3$ and CCH

We observed in DR21(OH) four lines of the $\nu_2$ fundamental band ($P(4)$, $Q(2)$, $Q(4)$ and $P(10)$), of triatomic carbon using the upper sideband of the HIFI bands 7a and 7b as well as the lower sideband of band 6b of the HIFI receiver. All $C_3$ spectra were observed at a single position in DR21(OH) with coordinates $\alpha$(J2000) = 20:39:01.00 $\delta$(J2000) = 42:22:48.0, in the dual beam switch mode. The observations were carried out on 2010 June 25 and November 25 to 27. The details of the observations and data reduction are given in Mookerjea et al. (2010). All spectra were smoothed to resolution between ~0.16 to 0.18 km s$^{-1}$, and the rms noise level for the spectra is 0.03 to 0.04 K. All the observed $C_3$ lines are at frequencies for which HEB mixers are used in HIFI, and we noticed a variation in the level of the continuum observed for different LO settings and polarizations for a particular spectral line. In the results presented here, there is only a shift in the continuum level, with little or no change in the depth of absorption. We verified that this shift in the continuum level does not arise from differences in the pointing of the telescope or the notorious HEB-band standing waves. We find the uncertainty in the continuum level to be most pronounced
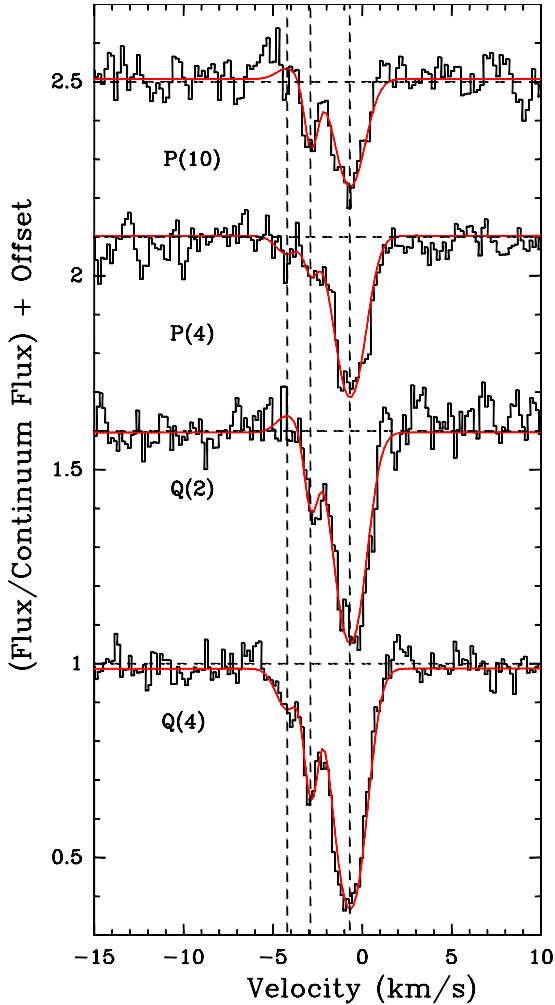
**Fig. 1.** HIFI observations of the C$_3$ lines in DR21(OH). The spectra are corrected for the DSB continuum and normalized to the SSB continuum level. The $Q(2)$, $P(4)$, and $P(10)$ spectra are shifted consecutively by +0.5, so that the plots do not overlap. The red line shows the simultaneous fit with three Gaussian velocity components (at −0.7, −2.9, and −4.2 km s$^{-1}$). Note that the third component is only detected above the noise in $Q(4)$ and $P(4)$. The "negative" absorption bumps at this velocity fitted in $Q(2)$ and $P(10)$ are within the noise.

for the $P(4)$ line at 1787 GHz. We evaluated the effect of these variations and included them in our estimate of uncertainties of the column densities (Sect. 3.1).

Figure 1 shows the observed spectra normalized to the (single sideband) continuum level. The observed C$_3$ absorption features occur around the systemic velocity (∼−1 km s$^{-1}$) of an infalling subfilament on DR21(OH) (see Schneider et al. 2010) and hence are associated with the source only and not with foreground material. The PRISMAS observations are not sensitive enough to detect C$_3$ lines in absorption in the diffuse gas along the line of sight to DR21(OH) (Mookerjea et al. 2010).

As part of the PRISMAS program, a large number of emission lines falling within the multiple observed bands were found, in addition to the target lines detected in absorption towards DR21(OH).

Here we use the two spectral lines of CCH at 523.97 and 524.03 GHz in DR21(OH) in HIFI Band 1a.

Table 2 summarizes the spectroscopic parameters of the species and transitions observed with *Herschel*.

## 2.2. IRAM 30 m data: CCH and c-C$_3$H$_2$

The ground state transition of CCH at 87.316 GHz ($N = 1$–0, $J = 3/2$–1/2, with three hyperfine components) and the $2_{1,2}$–$1_{0,1}$ transition of c-C$_3$H$_2$ at 85.338 GHz were observed by Gerin et al. (2011) using the IRAM-30 m telescope in 2006, August and December. Table 3 presents both spectroscopic and observational parameters of the lines observed with IRAM 30 m. The primary aim of these observations was the study of CCH and c-C$_3$H$_2$ in the diffuse and translucent clouds along the line of sight to DR21(OH). However, as do the HIFI data, these observations also detect the emission lines arising from the source DR21(OH) itself.

## 2.3. Position of beams relative to the continuum sources in DR21(OH)

Figure 2 presents the 12″ (C$_3$) and 43″ (CCH at 522 GHz) beams of HIFI and the 29″ IRAM 30 m beams overlaid on the images of 3 mm and 450 $\mu$m continuum emission from DR21(OH). The 3 mm continuum emission (color and black contours) was observed with PdBI (Csengeri et al. 2011), and the 450 $\mu$m (yellow contour) continuum data were obtained from the JCMT archives. We see that the 3 mm interferometric map (restored to a beam of 2″) clearly resolves the continuum sources MM1 and MM2 and also shows evidence for extended emission from the envelope. At a resolution of 8″, the 450 $\mu$m JCMT data shows that the continuum emission is primarily dominated by the surrounding extended envelope. The C$_3$ beam of HIFI covers a significant part of the source MM2 as well. The 29″ IRAM 30 m beam almost completely covers the larger region sampled by the 522 GHz HIFI beam. Thus, Fig. 2 shows that the observing beams for all the spectral observations presented in this paper cover regions including MM1, MM2, and the surrounding envelope. The spectral indices of the continuum emission derived so far from the 3 mm (PdBI) and 1.4 mm (SMA Zapata et al. 2012) data are not consistent with thermal emission from dust. It is thus difficult to characterize the contribution of MM1 and MM2 to the continuum emission. However, at the beam sizes of our C$_3$ observations at THz frequencies, it is probable that the continuum is dominated by the emission from the extended envelope and hence variation due to the contribution of the individual sources is likely to be small. We thus assume that all the C$_3$ absorption is of the same continuum, produced primarily from the extended envelope.

## 3. Results

### 3.1. C$_3$ column densities

The observed C$_3$ absorption spectra show evidence of multiple velocity components (Fig. 1). The $Q(4)$ transition clearly shows three velocity components, while the other transitions distinctly show two components. In a global fitting scheme, we assumed that each C$_3$ transition has contributions from three velocity components and then fitted all observed transitions simultaneously using multi-component Gaussians. The parameters fitted simultaneously in each transition are the common $v_{\rm LSR}$, $\Delta v$ for each of the three velocity components and the strength of the absorption dips, separately for each line. We thus assumed all three velocity components to be present in all transitions, even if the components are not explicitly seen, since we attribute the non-detection to the lower strength of the transition relative to the achieved rms of our observations rather than to any physical

**Table 2.** Spectroscopic parameters for the $C_3$ and CCH transitions observed with *Herschel*/HIFI.

| Species | Transition | Frequency (MHz) | $A$-coeff ($s^{-1}$) | $E_l$ ($cm^{-1}$) | Beam size |
|---|---|---|---|---|---|
| $C_3$, $(J, v)$ | $(9, 1)$–$(10, 0)$ P(10) | 1 654 081.66 | $2.38 \times 10^{-3}$ | 47.3 | 13″ |
| | $(3, 1)$–$(4, 0)$ P(4) | 1 787 890.57 | $2.72 \times 10^{-3}$ | 8.6 | 12″ |
| | $(2, 1)$–$(2, 0)$ Q(2) | 1 890 558.06 | $7.51 \times 10^{-3}$ | 2.6 | 11″ |
| | $(4, 1)$–$(4, 0)$ Q(4) | 1 896 706.56 | $7.58 \times 10^{-3}$ | 8.6 | 11″ |
| CCH, $N_{J,F}$ | $6_{13/2,7}-5_{11/2,6}$ | 523 971.5704 | $4.58 \times 10^{-4}$ | 43 | 40″ |
| | $6_{13/2,6}-5_{11/2,5}$ | 523 972.1630 | $4.53 \times 10^{-4}$ | 43 | 40″ |
| CCH, $N_{J,F}$ | $6_{11/2,6}-5_{11/2,5}$ | 524 033.9075 | $4.51 \times 10^{-4}$ | 43 | 40″ |
| | $6_{11/2,5}-5_{9/2,4}$ | 524 034.5305 | $4.43 \times 10^{-4}$ | 43 | 40″ |

**Notes.** [*] *Herschel*/HIFI beam sizes are taken from Roelfsema et al. (2012).

**Table 3.** Spectroscopic and observational parameters for the transitions of CCH and $c$-$C_3H_2$ observed with IRAM 30 m.

| Species | Transition | Frequency (MHz) | $A$-coeff ($s^{-1}$) | $E_l$ ($cm^{-1}$) | $\theta_{FWHM}$ (″) | $F_{eff}$[a] | $B_{eff}$[b] |
|---|---|---|---|---|---|---|---|
| CCH, $N_{J,F}$ | $1_{3/2,1}-0_{1/2,1}$ | 87 284.1050 | $2.60 \times 10^{-7}$ | 0.0015 | 29″ | 0.95 | 0.75 |
| | $1_{3/2,2}-0_{1/2,1}$ | 87 316.8980 | $1.53 \times 10^{-6}$ | 0.0015 | 29″ | 0.95 | 0.75 |
| | $1_{3/2,1}-0_{1/2,0}$ | 87 328.5850 | $1.27 \times 10^{-6}$ | 0.0015 | 29″ | 0.95 | 0.75 |
| $c$-$C_3H_2$, $(J_{K_a}, K_c)$ | $2_{1,2}-1_{0,1}$ | 85 338.8930 | $2.32 \times 10^{-5}$ | 1.7 | 29″ | 0.95 | 0.75 |

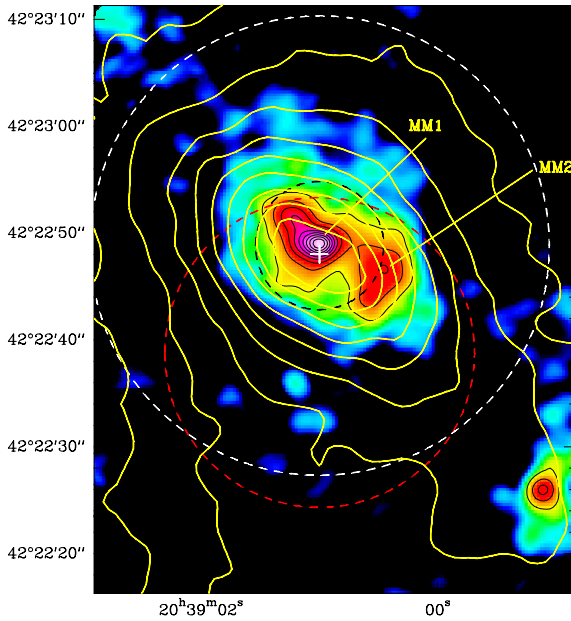**Notes.** [a] $F_{eff}$ forward efficiency and [b] $B_{eff}$ beam efficiency of the telescope.



**Fig. 2.** The 3 mm PdBI continuum image of DR21(OH) in color and black contours overlaid with yellow contours of 450 $\mu$m image observed with JCMT SCUBA. Also overlaid on the continuum image are the FWHM beam sizes for spectroscopic observations. The dashed lines show the HIFI (12″, black, and 43″, white) and IRAM 30 m (29″, red) beams. The white cross denotes the center of the HIFI beams.

or chemical reason. All four spectra show evidence of two major velocity components centered at $v_{LSR} = -2.85 \pm 0.04$ km s$^{-1}$ and $v_{LSR} = -0.68 \pm 0.02$ km s$^{-1}$, with the latter component being stronger. The third velocity component detected only in $Q(4)$ and marginally in the $P(4)$ spectra is at $-4.2 \pm 0.2$ km s$^{-1}$. We checked that for a particular transition in which the third component is undetected the results of fitting do not change significantly for the well-detected velocity components assuming the

presence of the third component. Table 4 presents the single sideband continuum levels (estimated from double sideband temperatures assuming a sideband gain ratio of 1) and the results of the Gaussian fit along with their uncertainties.

We compare the velocity components at $-0.7$, $-2.9$ km s$^{-1}$, and $-4.2$ km s$^{-1}$ with the known velocities in the region. The LSR velocities of the sources MM1 and MM2 are $-4.1$ and $-0.7$ km s$^{-1}$, respectively, and the peak of $C^{18}O$ emission is observed to have a $v_{LSR}$ of $-3.2$ km s$^{-1}$ at a resolution of 12″, which most likely arises from the envelope surrounding MM1 and MM2 (Mangum et al. 1992; Wilson & Mauersberger 1990). Our observation is centered on MM1; MM2, located 8″3 away from MM1, lies within the HIFI beam. Thus, although we cannot resolve MM1 and MM2 spatially, the velocities of the two sources and the envelope differ sufficiently from one another to allow identification of the three components in the $C_3$ spectra. We detect $C_3$ absorption due to MM2 and the envelope in all transitions, while MM1 appears only in the stronger $Q(4)$ transition and marginally in $P(4)$ transition. Based on the $J = 4$ column densities derived for the $-4.2$ km s$^{-1}$ component assuming $T_{rot}$ between 50–70 K, we estimate the expected absorption depths for the $J = 2$ level to be only 10% and even less for the $J = 10$ level; this is comparable to the uncertainty in our measurements. Thus, the nondetection of the $-4.2$ km s$^{-1}$ component in $Q(2)$ and $P(10)$ is consistent with the expected strengths of these lines.

Taking into consideration the uncertainties in the measurements described above, we estimate the state-specific column densities to be $\sim 10^{14}$ cm$^{-2}$ and $\sim 10^{13}$ cm$^{-2}$ for the $-0.7$ km s$^{-1}$ and $-2.9$ km s$^{-1}$ components, respectively (Table 4). For $Q(4)$ and $P(4)$, and the additional absorption feature at $-4.2$ km s$^{-1}$ corresponds to a $J = 4$ column density of $\sim 10^{13}$ cm$^{-2}$. Given the marginal detection at $P(4)$ and nondetection at $Q(2)$, we propose the $J = 4$ column density for the $-4.2$ km s$^{-1}$ component to be an upper limit. Using the $J = 2$, 4, and 10 levels, we construct rotation diagrams and obtain rotation temperatures

**Table 4.** Single sideband continuum antenna temperatures ($T_c$) and parameters derived from simultaneous Gaussian fitting of all the line profiles and the lower state C$_3$ column densities ($N_l$) estimated from the fitted intensities.

| Transition | $T_c$ [K] | $V_{cen}$ [km s$^{-1}$] | $\int \tau \mathrm{d}v$ [km s$^{-1}$] | $N_l$ [10$^{14}$ cm$^{-2}$] |
|---|---|---|---|---|
| $P(10)$ | $7.1 \pm 0.4$ | $-0.7$ | $0.60 \pm 0.07$ | $1.2 \pm 0.08$ |
| | | $-2.9$ | $0.17 \pm 0.04$ | $0.3 \pm 0.06$ |
| | | $-4.2$ | ... | ... |
| $P(4)$ | $7.0 \pm 1.3$ | $-0.7$ | $1.00 \pm 0.06$ | $2.5 \pm 0.1$ |
| | | $-2.9$ | $0.08 \pm 0.03$ | $0.2 \pm 0.07$ |
| | | $-4.2$ | $0.07 \pm 0.03$ | $0.17 \pm 0.08$ |
| $Q(2)$ | $7.1^{+0.6}_{-0.5}$ | $-0.7$ | $1.46 \pm 0.05$ | $1.2 \pm 0.06$ |
| | | $-2.9$ | $0.19 \pm 0.03$ | $0.2 \pm 0.04$ |
| | | $-4.2$ | ... | ... |
| $Q(4)$ | $6.7^{+0.3}_{-0.7}$ | $-0.7$ | $1.79 \pm 0.04$ | $1.5 \pm 0.06$ |
| | | $-2.9$ | $0.33 \pm 0.03$ | $0.3 \pm 0.03$ |
| | | $-4.2$ | $0.16 \pm 0.03$ | $0.1 \pm 0.06$ |
| Total$^a$ | | $-0.7$ | ... | $9.1 \pm 2.3$ |
| | | $-2.9$ | ... | $2.2 \pm 0.4$ |

**Notes.** The error bars in $N_l$ include errors due to both uncertainty in the continuum level and the line-fitting procedure. The velocity components are as follows: component 1: $v_{cen} = -0.68 \pm 0.02$ km s$^{-1}$, $\Delta V = 1.85 \pm 0.51$ km s$^{-1}$, component 2: $v_{cen} = -2.85 \pm 0.04$ km s$^{-1}$, $\Delta V = 0.86 \pm 0.08$ km s$^{-1}$, and component 3: $v_{cen} = -4.2 \pm 0.2$ km s$^{-1}$, $\Delta V = 1.4 \pm 0.4$ km s$^{-1}$. Velocity component 3 is detected only above the noise level in $P(4)$ and $Q(4)$. $^{(a)}$ Estimated using rotation diagram (Fig. 3).

of $76 \pm 20$ K and $48 \pm 6$ K for the velocity components at $-2.9$ km s$^{-1}$ and $-0.7$ km s$^{-1}$, respectively (Fig. 3). The total C$_3$ column densities for the $-2.9$ km s$^{-1}$ and $-0.7$ km s$^{-1}$ components are $(2.2 \pm 0.4) \times 10^{14}$ cm$^{-2}$ and $(9.1 \pm 2.3) \times 10^{14}$ cm$^{-2}$, respectively. Thus, the $-0.7$ km s$^{-1}$ component corresponds to the colder and higher column density gas.

## 3.2. CCH column densities

In the PRISMAS observations we detected five transitions of CCH at frequencies around 87.3 GHz and 524.0 GHz. We first attempted to derive a self-consistent LTE model, which explains the intensities of all the CCH transitions using a combination of XCLASS (Schilke et al. 1999; Comito et al. 2005) and MAGIX (Bernst et al. 2011). XCLASS generates synthetic spectra consisting of multiple velocity components as well as hyperfine structure components for all transitions of different chemical species. XCLASS accesses the molecular databases CDMS and JPL and models each molecule with the following free parameters: source size, temperature, column density, line width and velocity offset relative to the systemic velocity of the source. It also derives the column density corresponding to the different velocity components detected in absorption and emission in the observed spectra. The source size refers to the size of the cloud contributing to the emission or absorption spectra. The synthetic spectra generated with XCLASS were fitted to the observed spectra using MAGIX, an iterating engine that allows automatic minimization to constrain model parameters. We assumed that the hyperfine lines have the same excitation temperatures. We note that the fitting procedure can involve considerable degeneracy between source size, excitation temperature and column
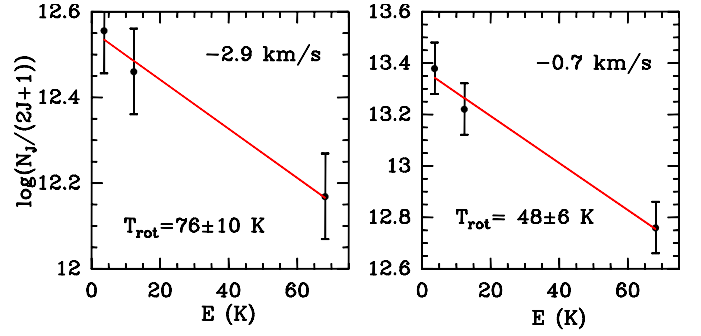


**Fig. 3.** Rotation diagram of C$_3$ for the velocity components at $-0.7$ km s$^{-1}$ and $-2.9$ km s$^{-1}$. The errorbars correspond to an estimated error of 10% in the state specific column densities and are conservative estimates, which include uncertainties due to continuum measurements as well as the noise in the spectra.

density. In the absence of more accurate information, we fixed the source sizes for MM1 and MM2 to 15″ and the size for the envelope to 30″. Using XCLASS/MAGIX we could not obtain an LTE model that consistently explained the intensities of all five lines of CCH. We found that the 87 GHz lines have intensities much higher than the expected values based on the 524 GHz intensities under the assumption of LTE. We thus fitted two different LTE models to the 87 GHz and 524 GHz spectra of CCH. Figures 4a and b show the observed CCH spectra along with the LTE models fitted using XCLASS; the fit parameters are presented in Table 5. The errorbars for the parameters in Table 5 represent the range of values over which the best-fit model does not change significantly.

From the intensities of the 87.316 GHz CCH lines, we estimate the LTE temperatures of the $-0.5$, $-2.9$, and $-4.2$ km s$^{-1}$ components contributing to the CCH emission to be 110 K, 9 K, and 111 K, respectively. The CCH transition at 524 GHz shows evidence of only two velocity components at $-2.8$ km s$^{-1}$ and $-4.6$ km s$^{-1}$, with temperatures of 33 K and 101 K respectively.

While the temperatures of the envelope derived from the LTE models of the 87 GHz and the 524 GHz transitions are not too discrepant, the total CCH column densities of the envelope ($v_{cen} = -2.7$ km s$^{-1}$) estimated from the two transitions are $2.3 \times 10^{15}$ cm$^{-2}$ and $2.9 \times 10^{14}$ cm$^{-2}$, respectively, hence differing by a factor ~8. This discrepancy in column densities indicates two possibilities. First, it is likely that the excitation of CCH is non-LTE, so while the 87 GHz transition with a low critical density is thermalized and traces the total column density better, a commensurate number of molecules in the higher energy levels probed by the 524 GHz lines are not present. Second, owing to the difference in the pointing centers of the beams the 87 GHz data could also be tracing the emission from the extended ridge in DR21(OH), whereas the higher-$J$ lines at 524 GHz primarily trace the DR21(OH) hot core and the envelope. Though difficult to quantify, the difference in coupling of the emission with the beams at 87 and 524 GHz, which are of different sizes and differently centered, could contribute to part of the discrepancy. For consistent comparison of the abundances of CCH, $c$-C$_3$H$_2$ and C$_3$ in the envelope, we use the column densities derived from the 87 GHz CCH transitions as an upper limit for chemical models discussed later.

## 3.3. LTE modeling of c-C$_3$H$_2$

We also derived an LTE model for the single $c$-C$_3$H$_2$ line using a two-component Gaussian profile corresponding to the velocities
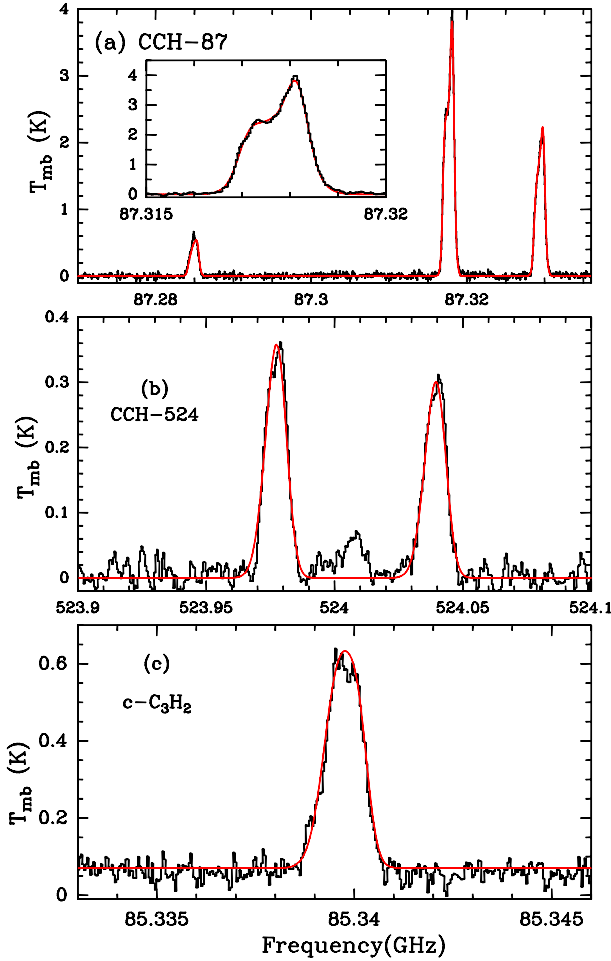
**Fig. 4.** Spectra of **a)** CCH at 87.316 GHz, **b)** CCH at 523.9 GHz, and **c)** $C_3H_2$ at 85.338 GHz fitted with LTE models using XCLASS. The spectra of (a) also show the main hyperfine component of 87.316 GHz as inset to demonstrate the velocity structure better.

**Table 5.** Parameters derived from fitting the CCH (observed with HIFI and IRAM) and $c$-$C_3H_2$ lines with LTE models using XCLASS.

| Species | Size $''$ | $T$ K | $N$ $10^{14}$ cm$^{-2}$ | $\Delta v$ km s$^{-1}$ | $v_{LSR}$ km s$^{-1}$ |
|---|---|---|---|---|---|
| CCH-87 | 15 | $110 \pm 15$ | $19.7 \pm 3.0$ | $1.6 \pm 0.1$ | $-0.6 \pm 0.1$ |
| | 30 | $9 \pm 2$ | $23.4 \pm 1.3$ | $3.5 \pm 0.1$ | $-2.7 \pm 0.1$ |
| | 15 | $111 \pm 10$ | $60.3 \pm 4.0$ | $1.7 \pm 0.1$ | $-4.2 \pm 0.1$ |
| CCH-524 | 30 | $33 \pm 5$ | $1.2 \pm 0.3$ | $5.5 \pm 0.2$ | $-2.8 \pm 0.2$ |
| | 15 | $101 \pm 11$ | $1.4 \pm 0.3$ | $4.5 \pm 0.2$ | $-4.6 \pm 0.2$ |
| $C_3H_2$ | 30 | $31 \pm 4$ | $0.7 \pm 0.1$ | $3.3 \pm 0.1$ | $-2.7 \pm 0.1$ |
| | 15 | $78 \pm 6$ | $0.9 \pm 0.2$ | $1.5 \pm 0.2$ | $-4.5 \pm 0.2$ |

**Notes.** Parameters without errorbars were held constant for the fitting.

around $-2.7$ km s$^{-1}$ and $-4.5$ km s$^{-1}$. Figure 4c shows the observed $c$-$C_3H_2$ spectrum fitted with a two-component model using XCLASS.

### 3.4. Temperature structure in DR21(OH)

Based on the results of synthesis imaging of thermal NH$_3$ and detection of the (7, 7) transition of NH$_3$, which is 535 K above

**Table 6.** Comparison of observed abundances of the chemical species in the envelope of DR21(OH) and other sources.

| Species | DR21(OH) | | Lukewarm corino[b] | Hot corino[c] |
|---|---|---|---|---|
| | $N$ cm$^{-2}$ | $X^a$ $\times 10^{-9}$ | $X$ $\times 10^{-9}$ | $X$ $\times 10^{-9}$ |
| $C_3$ | $2.2 \times 10^{14}$ | 0.63 | … | … |
| CCH (87 GHz) | $2.3 \times 10^{15}$ | 6.6 | (5.3–12.8) | 0.05 |
| CCH (524 GHz) | $2.9 \times 10^{14}$ | 0.8 | (5.3–12.8) | 0.05 |
| $c$-$C_3H_2$ | $6.8 \times 10^{13}$ | 0.19 | 0.22 | …[d] |

**Notes.** [a] Estimated using $N(H_2) = 3.5 \times 10^{23}$ cm$^{-2}$ (Table 1). [b] Sakai et al. (2009a,b). [c] Sakai et al. (2009a); Cazaux et al. (2003); Bisschop et al. (2007). [d] Observations not available, Hassel et al. (2011) model ($n_{H_2} = 5 \times 10^5$ cm$^{-3}$) predicts X($c$-$C_3H_2$) $\approx 10^{-9}$ in lukewarm corinos ($T \sim 30$ K) and X($c$-$C_3H_2$) $\approx 10^{-7}$ in hot cores ($T \sim 100$ K).

the ground state, the kinetic temperature of the gas associated with MM1 ($v_{LSR} = -4.1$ km s$^{-1}$) is estimated to be >80 K (Mangum et al. 1992; Mauersberger et al. 1986). Wilson & Mauersberger (1990) derived a kinetic temperature of 34 K for this region using NH$_3$ observations at a resolution of 40″.

We note that the 43″ beam size for the 524 GHz HIFI observations and the 29″ beam size of IRAM 30 m (Fig. 2) include MM1, MM2, and the envelope. Hence, the observed CCH emission is primarily due to the molecular gas surrounding all these sources, which is traced in CO and C$^{18}$O. Using CCH and $c$-$C_3H_2$, we derive the temperature of the component corresponding to the envelope to be 10–30 K and the temperature of the component associated with MM1 to be 100–110 K. The data on carbon chain molecules are consistent with the presence of high temperatures in MM1 and MM2 and agree with the previous determinations.

## 4. Modeling observed chemical abundances in the envelope

### 4.1. The OSU gas-grain models

We model the observed abundances of the three chemical species $C_3$, $c$-$C_3H_2$, and CCH (Table 6) in the warm envelope around DR21(OH) using the Ohio State University (OSU) gas-grain code with a warm-up (Hasegawa et al. 1992; Garrod & Herbst 2006). Although slightly shifted in velocity from the envelope at $-4.2$ km s$^{-1}$ detected in $C_3$ for CCH-524 and $c$-$C_3H_2$, we consider the $-4.5$ km s$^{-1}$ velocity component to correspond to the envelope. Since the models are primarily for dense star-forming regions and the low-frequency CCH transition (87 GHz) likely traces an additional extended component, we use the CCH abundance derived from the IRAM data as an upper limit to compare with the outcome of the model. Motte et al. (2007) estimated the average volume density of the entire region to be $10^6$ cm$^{-3}$, while the MM1 and MM2 dense cores reach densities larger than $10^7$ cm$^{-3}$ (Table 1). Thus, for the envelope we presently consider models with constant gas densities $n_{H_2} = 5 \times 10^5$, $1 \times 10^6$, and $5 \times 10^6$ cm$^{-3}$.

The gas-grain network considers 7166 reactions involving a total of 668 gaseous and surface species, where the surface species are identified with (s). The physical parameters and initial chemical abundances adopted are the same as used by

**Table 7.** Parameters for the models explored for C$_3$ chemistry in DR21(OH).

| Model | $T_{max}$ (K) | $n_{H_2}$ (cm$^{-3}$) |
|-------|------|------|
| 1 | 30 | $5 \times 10^5$ |
| 2 | 30 | $1 \times 10^6$ |
| 3 | 30 | $5 \times 10^6$ |
| 4 | 50 | $5 \times 10^5$ |
| 5 | 50 | $1 \times 10^6$ |
| 6 | 50 | $5 \times 10^6$ |

**Table 8.** Parameters assumed to remain constant in present models.

| Parameter | Value | Unit |
|-----------|-------|------|
| [b] Cosmic Ray Ionization Rate $\zeta$ | $1.3 \times 10^{-17}$ | s$^{-1}$ |
| [b] Visual Extinction $A_V$ | 10 | |
| [a,b] Grain Radius $a_d$ | $1 \times 10^{-5}$ | cm |
| [a,b] Nonthermal Desorption Yield $a_{RRK}$ | 0.01 | |
| [a,b] Initial Temperature $T_i$ | 10 | K |
| [a,b] Warm-up Timescale $t_{sc}$ [a,b] | $2 \times 10^5$ | yr |
| [b] Warm-up Offset Time $t_{off}$ | $1 \times 10^5$ | yr |

**Notes.** [a] Garrod & Herbst (2006); [b] Hassel et al. (2008).

Garrod et al. (2007) and Hassel et al. (2008, Tables 1 and 2). In this approach, a one-point parcel of material undergoes an initially cold period of $T_0 = 10$ K with a duration of $t = 10^5$ yr, followed by a gradual temperature increase. A heating timescale of $t_h = 0.2$ Myr is adopted following Garrod & Herbst (2006), where we use values for the maximum temperature $T_{max}$ of 30 K and 50 K, so that the model reaches $T_{max}$ by $t \approx 0.3$ Myr. A total of six combinations of $T_{max}$ and $n_{H_2}$ are considered, as outlined in Table 7. In contrast to more complex hydrodynamic approaches (Aikawa et al. 2008), the other physical parameters here (Table 8) are assumed to be homogeneous at any given time and from one model to another. The advantage of this approach is that it allows a more detailed look at the chemical processes and the roles of individual reactions. A similar procedure was previously used to simulate the formation of hydrocarbon chains in the envelopes of low-mass protostellar envelopes by Hassel et al. (2008) and Hassel et al. (2011), where the latter model also considered the linear C$_3$ toward W31C and W49N (Mookerjea et al. 2010).

The models include photodesorption rates for CO(s), N$_2$(s), H$_2$O(s), and CO$_2$(s) based on the measurements of Öberg et al. (2007, 2009a,b). The adopted processes and rates are species-dependent, rather than dependent on a single parameter.

The production of hydrocarbon chains during the warm-up has been attributed to a process beginning with grain surface chemistry. The elevated temperature allows methane to evaporate from the ice mantles surrounding dust particles and act as a precursor for a carbon-chain rich ion-molecule chemistry. Hassel et al. (2011, Fig. 6) demonstrated that the abundance of C$_3$ is subject to such a process. In particular, the C$_3$ is formed via gas phase chemistry involving atomic C at early times and depletes sharply at $t \sim 10^5$ yr, after which time most available atomic C is incorporated into CO. In the absence of grain surface chemistry, the C$_3$ will continue to deplete to abundances below $10^{-12}$ by 1 Myr. In models including grain surface chemistry, the abundance of C$_3$ is regenerated following the release of CH$_4$(s) and subsequent gas phase chemistry during the warm-up. The abundances and reactions discussed in this section refer to the gas phase.

### 4.2. Model results

The time evolution of fractional abundances is presented for C$_3$, CCH and $c$-C$_3$H$_2$ in Fig. 5, along with the corresponding observed values. In all models, the warm-up occurs between 0.1 and 0.3 Myr starting from an initial temperature of 10 K, similar to the temperature profiles that appear in Hassel et al. (2008, Figs. 2 and 3). We observe the following general trends in the abundance profiles shown in Fig. 5: for the lower temperature models (1–3), the molecular abundances attain values comparable to the observed abundances for a much longer period of time as compared to the higher temperature models (4–6). Further,

for both C$_3$ and $c$-C$_3$H$_2$ in models 4–6, the maximum abundance decreases with increasing values of $n_{H_2}$.

Figure 5 shows that all six models produce CCH to a peak abundance of $X = 0.2–1 \times 10^{-8}$ during the warm-up. The abundance depletes more rapidly for models 4–6, while the abundance remains elevated for a longer period for models 1−3. Moreover, higher densities produce a slightly smaller CCH abundance following the warm-up. The C$_3$ abundance depletes more rapidly for models 4–6, and smaller abundances are produced for larger density during this period. All the models produce a similar abundance of $c$-C$_3$H$_2$ in the range of $X = 0.5−1 \times 10^{-8}$ following the warm-up. The temperature and density effects seen in the previous two species also appear for $c$-C$_3$H$_2$ but to a lesser extent.

The primary reason for the difference in abundance of the chemical species considered here for $T_{max} = 30$ K and 50 K models is that the higher temperature will release additional species from the icy grain mantles to the gas. This leads to additional, competitive reaction pathways with the overall effect of a comparative depletion of abundance of these particular species. A similar effect is visible at the onset of the warm-up, when the abundances of the three species deplete sharply just prior to the steep increase attributed to the warm-up.

### 4.3. Major chemical reactions

Table 9 summarizes the most important chemical reactions occurring in the gas phase during warm-up as determined by the gas-grain chemistry model (Garrod & Herbst 2006). We emphasize that the species produced here also result from other ion-molecule reactions and that Table 9 lists only the most direct and salient mechanisms. The liberated CH$_4$ reacts with C$^+$ to form the intermediate species C$_2$H$_2^+$ and C$_2$H$_3^+$ via reactions (1) and (3). Subsequently, the reaction of H$_2$ with C$_2$H$_2^+$ in (2) produces C$_2$H$_4^+$. The dissociative recombination reaction of an electron with these intermediate ions then produces C$_2$H$_2$ by reaction (2) or reaction (5). Further reactions of CH$_4$ with the intermediate ions can produce C$_3$H$_5^+$ via reactions (6) and (7), while the dissociative recombination of C$_3$H$_5^+$ produces C$_3$H$_3$ via reaction (8). Reactions of C and C$^+$ with C$_2$H$_2$ (9, 11) produce C$_3$H and C$_3$H$^+$. Further reaction of these products (12, 13) produce C$_3$H$_2^+$, and the reaction of CH$_4$ with C$_3$H$_2^+$ (14) produces C$_3$H$_3^+$. The C$^+$ and C result from partial desorption of CO(s) and subsequent reaction with He$^+$ during the warm-up. These represent the major precursors for the observed species and provide the basis to examine each species individually.

For the chemical species considered here, we identify the primary formation reactions as follows: CCH is primarily formed by the dissociative recombination of C$_2$H$_3^+$ in reaction (17). The evolution of C$_3$ proceeds in a somewhat different manner.
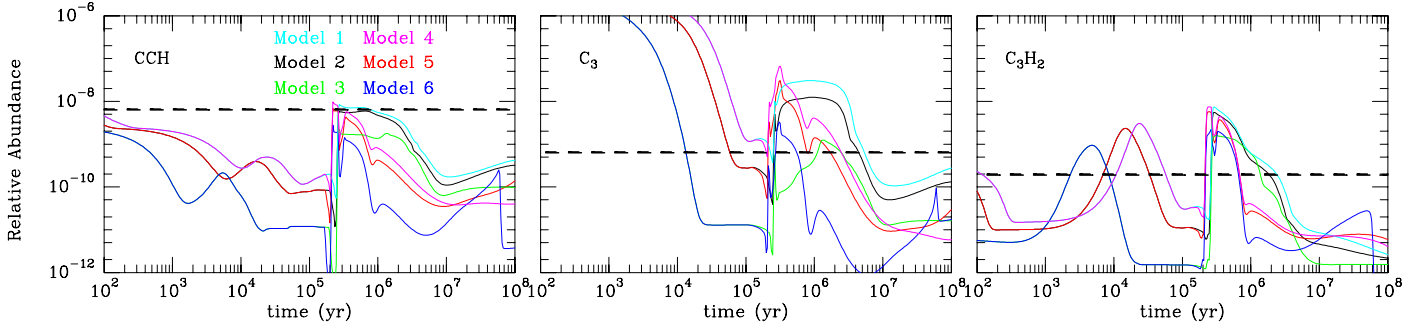
**Fig. 5.** Comparison of observed abundances in the envelope (shown by dashed lines) with the results of chemical models involving warming up of grains for different combinations of hydrogen density ($n_{H_2}$) and final warm-up temperatures. The model calculates abundances relative to hydrogen, and the observed column densities of the different species have been converted to fractional abundances assuming $N(H_2) = 3.5 \times 10^{23}$ cm$^{-2}$. In all models, the warm-up occurs between 0.1 and 0.3 Myr starting from an initial temperature of 10 K, similar to the temperature profiles that appear in Hassel et al. (2008, Figs. 2 and 3).
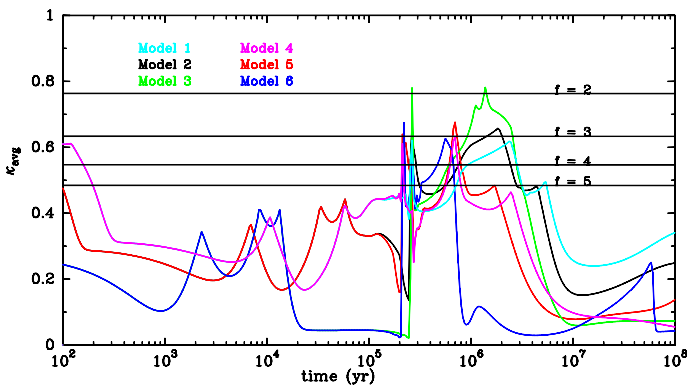


**Fig. 6.** Mean confidence level $\kappa_{avg}$ calculated for the chemical models as explained in the text (Garrod et al. 2007).

Ion-molecule chemistry forms a relatively large abundance of this species at early times, followed by a depletion to grain surfaces. This depletion happens at slightly earlier times for models with larger values of density. Although C$_3$ is frozen on the dust grains, it is not liberated directly from the grains during the warm-up, but rather is produced in a reaction sequence starting with CH$_4$. The C$_3$(s) however is more likely to participate in surface reactions than to desorb. The reaction of C + C$_2$H$_2$ produces C$_3$ through reaction (19). This mechanism and the secondary pathways result in the formation of a peak in the abundance during and after the warm-up period. The formation of $c$-C$_3$H$_2$ can proceed via three pathways. The first mechanism is reaction (21), in which C$_3$H$_3$ reacts with H. The dissociative recombination of C$_3$H$_3^+$ (22) is a second mechanism. Alternatively, reaction (23) of CH with C$_2$H$_2$ is another important formation pathway.

### 4.4. Best fit chemical model

In order to compare model results with observations on a more quantitative basis, we compute the mean confidence level (Garrod et al. 2007) during the warm-up period. In this quasi-statistical analysis introduced by Garrod et al. (2007), the confidence level, $\kappa_i$, for agreement between computed and observed abundances is defined as

$$\kappa_i = erfc\left(\frac{|\log(X_i) - \log(X_{obs,i})|}{\sqrt{(2)}\sigma}\right). \qquad (1)$$

**Table 9.** Dominant reactions of observed and intermediate species following CH$_4$ sublimation.

| | | | | | | | |
|---|---|---|---|---|---|---|---|
| | | | C$_2$H$_2$: | | | | |
| 1.) | C$^+$ | + | CH$_4$ | → | C$_2$H$_3^+$ | + | H |
| 2.) | C$_2$H$_3^+$ | + | e | → | C$_2$H$_2$ | + | H |
| 3.) | C$^+$ | + | CH$_4$ | → | C$_2$H$_2^+$ | + | H$_2$ |
| 4.) | C$_2$H$_2^+$ | + | H$_2$ | → | C$_2$H$_4^+$ | | |
| 5.) | C$_2$H$_4^+$ | + | e | → | C$_2$H$_2$ | + | 2 H |
| | | | C$_3$H$_3$: | | | | |
| 6.) | C$_2$H$_3^+$ | + | CH$_4$ | → | C$_3$H$_5^+$ | + | H$_2$ |
| 7.) | C$_2$H$_2^+$ | + | CH$_4$ | → | C$_3$H$_5^+$ | + | H |
| 8.) | C$_3$H$_5^+$ | + | e | → | C$_3$H$_3$ | + | H$_2$ |
| | | | C$_3$H$_3^+$: | | | | |
| 9.) | C | + | C$_2$H$_2$ | → | C$_3$H | + | H |
| 10.) | HCO$^+$ | + | C$_3$ | → | C$_3$H$^+$ | + | CO |
| 11.) | C$^+$ | + | C$_2$H$_2$ | → | C$_3$H$^+$ | + | H |
| 12.) | HCO$^+$ | + | C$_3$H | → | C$_3$H$_2^+$ | + | CO |
| 13.) | C$_3$H$^+$ | + | H$_2$ | → | C$_3$H$_2^+$ | + | H |
| 14.) | C$_3$H$_2^+$ | + | CH$_4$ | → | C$_3$H$_3^+$ | + | CH$_3$ |
| 15.) | HCO$^+$ | + | $c$-C$_3$H$_2$ | → | C$_3$H$_3^+$ | + | CO |
| 16.) | C$_3$H$^+$ | + | H$_2$ | → | C$_3$H$_3^+$ | | |
| | | | CCH: | | | | |
| 17.) | C$_2$H$_3^+$ | + | e | → | **CCH** | + | 2 H |
| 18.) | HCO$^+$ | + | **CCH** | → | C$_2$H$_2^+$ | + | CO |
| | | | C$_3$: | | | | |
| 19.) | C | + | C$_2$H$_2$ | → | **C$_3$** | + | H$_2$ |
| 20.) | **CCH** | + | C$_3$ | → | C$_5$ | + | H |
| | | | $c$-C$_3$H$_2$: | | | | |
| 21.) | H | + | C$_3$H$_3$ | → | $c$-C$_3$H$_2$ | + | H$_2$ |
| 22.) | C$_3$H$_3^+$ | + | e | → | $c$-**C$_3$H$_2$** | + | H |
| 23.) | CH | + | C$_2$H$_2$ | → | $c$-C$_3$H$_2$ | + | H |
| 24.) | HCO$^+$ | + | $c$-C$_3$H$_2$ | → | C$_3$H$_3^+$ | + | CO |

**Notes.** The observed species are identified in bold type.

The index $i$ refers to individual chemical species under consideration. The mean of the individual values of $\kappa_i$ thus computed is denoted by $\kappa_{avg}$. Since we consider the computed abundance to "fit" the observation if the abundance agrees within an order of magnitude or better we assume $\sigma = 1$ so that one standard deviation corresponds to agreement of one order of magnitude. The related confidence level for such a factor of 10 agreement is $\kappa_i = 0.317$, and the value increases up to $\kappa_i = 1$ for closer

agreement. The accuracy of this analysis and the robustness of $\kappa_{avg}$ against individual values of $\kappa_i$ improve with increasing size of the considered dataset. Since we have considered only three chemical species, we use the $\kappa$-based analysis primarily as a guideline to identify models that best reproduce the data. The best fit corresponds to the maximum average confidence level.

Figure 6 shows the $\kappa_{avg}$ values for each model that we have considered here, along with horizontal lines indicating agreement within a factor ($f$) of 2, 3, 4, and 5. The primary interpretation of this diagram is that all six models reasonably fit the observed abundances during the period following the warm-up. Models 1–3 fit the observation set within a factor of 2–4 or better for the time period of $t \sim 0.7$–3 Myr for all three density values. Models 4–6 fit the observation set within a factor of 3–5 or better for the period of $t \sim 0.6$–0.8 Myr for models 4 and 5 and for the earlier period $t \sim 0.3$–0.7 Myr for model 6. Model 3 gives the best agreement with observations in terms of the value and duration of the $\kappa_{avg}$ function, while model 2 is the second best at meeting these criteria. This analysis quantitatively asserts the level of model agreement described in Fig. 5 and broadly shows that the best sustained agreement of the models occurs in the time following the warm-up, rather than earlier or later.

# 5. Discussion

## 5.1. Lower gas phase abundance of $C_3$ in MM1

The angular resolution of the spectroscopic observations used in this paper lies between 12 and 40″, so that MM1 and MM2, are not resolved spatially. However, due to their markedly different velocities, MM1, MM2, and the envelope are easily discernible in the spectra. Interestingly, all $C_3$ spectra show primarily two velocity components associated with MM2 and the envelope, with absorption due to MM1 being detected only in $Q(4)$. In contrast, the chemically related species CCH and $c$-$C_3H_2$ that we have considered here show components corresponding to only MM1 and the envelope. Thus, there is an intrinsic difference in the distribution of $C_3$ compared to the distribution of the other species. The abundance of $C_3$ in MM2 ($1.2 \times 10^{-9}$) is only twice that in the envelope ($6.3 \times 10^{-10}$). Based on Table 1, the total column density of MM1 is ∼60% of the column density of MM2. This suggests that if the relative abundances of $C_3$ in MM1 and MM2 were similar, the total column density of $C_3$ in MM1 would have been 2.5 times the column density in the envelope so that the absorption dips due to MM1 would be similar to or stronger than the dip due to the envelope. It may be argued that the continuum backgrounds for the two components MM1 and the envelope may be different. However the continuum from MM1 is expected to be stronger than the continuum from the envelope. All these arguments indicate that $C_3$ is preferentially depleted or destroyed in MM1.

One major difference between MM1 and MM2 lies in the fact that MM1 has already shown evidence for at least one high temperature hot core, whereas MM2, though more massive, shows no such components. The chemical network includes among others the reaction $C_3 + H_2 \rightarrow C_3H + H$ (Pineau des Forêts et al. 1988), which becomes a primary destruction pathway for $C_3$ when the temperature exceeds ≈80 K. As a result, models predict that $C_3$ will be depleted in favor of $c$-$C_3H_2$ in hot core conditions, as $C_3H$ is also destroyed by reaction with $H_2$. Additionally, the chemical models presented here also show that the $C_3$ abundance is reduced at larger densities. MM1 is definitely at a higher density than the envelope (Table 1), so that the reduced abundance of $C_3$ in MM1 relative to MM2 could also

indicate that MM2 has a density lower than MM1. We note that this contradicts the densities derived from dust column densities (Table 1), which is not completely unexpected since the densities derived from the column densities are beam averaged and need not always reflect the local densities in a region.

However, an alternate possibility arises from the fact that the source intrinsic continuum opacity can refill the absorption to a significant extent, so that the column densities derived here are all primarily lower limits (Mookerjea et al. 2010). It can thus be envisaged that in the case of MM1, which has a stronger continuum emission, it is a combination of the geometry of the source and the refilling of the absorption dip that reduces the "visibility" of $C_3$. A proper evaluation of the effect of the continuum opacity on the absorption depth is possible only by constructing a complete radiative transfer model of the entire region with accurate temperature and density profiles, which are not yet available.

Finally, since MM2 is estimated to be younger than MM1 and $c$-$C_3H_2$, and CCH emission from MM2 are not detected, the possibility that the observed $C_3$ abundance in MM2 is due to the pre-warm-up gas-phase chemistry can also not be ruled out.

## 5.2. Comparison with $C_3$ in diffuse clouds

In diffuse clouds $C_3$ has been found to have an almost one-to-one correlation with $C_2$ (Roueff et al. 2002). In addition, the abundance of $C_3$ in diffuse clouds, $(3$–$6) \times 10^{-9}$ (Roueff et al. 2002), is ten times larger than the abundance of $C_3$ derived in the dense star-forming environment of DR21(OH). Oka et al. (2003) had explained the observed correlation between $C_2$ and $C_3$ in diffuse clouds in terms of a direct pathway of formation of $C_3$ from $C_2$ (see their Fig. 4). In the previous section, we examined the formation of $C_3$ during a warm-up period and noted a relatively larger abundance of this species prior to $t = 10^5$ yr, the so-called "early time". We now explore the chemistry of $C_3$ in diffuse regions and during the early time period in dense gas regions in order to examine the differences (if any).

The first step of the transformation of $C_2$ to $C_3$ in diffuse clouds is the photoionization of $C_2$ to $C_2^+$ (Oka et al. 2003). In contrast, the models for the dense star-forming regions assume darker ($A_V = 10$) conditions, so photoionization is not an effective process.

In dense models, the process begins with the radiative association of $C^+ + H_2 \rightarrow CH_2^+$. Next, $CH_2^+$ reacts with $H_2$ to form $CH_3^+$. This is followed by the dissociative recombination of $CH_3^+$ and $CH_2^+$ as competitive reactions to form CH and then by an ion-neutral reaction with $C^+$ to form $C_2^+$. As shown in Fig. 4 of (Oka et al. 2003), the pathway subsequently follows along the upper ($C_2H$) branch to form $C_3$. The $C_3$ is destroyed by processes that form $C_4$, $C_4^+$, and $C_5$, which react further to primarily form $C_3$ in a cyclic process. The abundance of $C_3$ grows until $C^+$ is depleted at $t \sim 10$–100 yr, depending on the density, after which it reaches a plateau until the $C_3$ is accreted onto grain surfaces. Dissociative recombination reactions with $C_2H^+$, $C_2H_2^+$, and $C_3^+$ along the pathway form $C_2$. The $C_2$ then reacts with O to form CO, and the abundance consequently falls to $X(C_2) \sim 10^{-9}$, far below the $X(C_2):X(C_3) = 40 : 1$ measured by Oka et al. (2003) for diffuse clouds.

Thus, $C_2$ is not the starting point for $C_3$ formation in dense cloud models at early times and does not undergo a cycling process like that of $C_3$. As a result, the correlation between $C_2$ and $C_3$ abundance is not predicted by dark cloud models. Rather, the $C_2$ abundance evolution more closely follows the evolution of CCH from early times until the warm-up begins than that of $C_3$. This comparison indicates that the chemistry of $C_3$ formation in

the envelope of DR21(OH) is definitely not the same as in diffuse clouds. Furthermore, the early time abundance of $C_3$ for dense regions exceeds the observed abundance by three orders of magnitude, effectively excluding this formation route as well.

### 5.3. Warm carbon chain chemistry in the envelope

Comparison of the present model results and observations indicates that the observed composition can be simulated with ion-molecule chemistry following a moderate warm-up to 30–50 K. This also means that $C_3$ formation in star-forming regions can be explained in terms of the moderate temperature (30 K) gas-phase chemical reactions starting from $CH_4$ evaporated from the grain mantle only and thus does not require photochemistry of PAH molecules.

The observed abundances of $C_3$ are consistent with formation during a warm-up model, "warm carbon chain chemistry" (WCCC; Sakai et al. 2008), and are related to the abundances of CCH, $c$-$C_3H_2$. This suggests that the envelope conditions are more like those of "lukewarm corinos" surrounding low-mass protostars than those of hot cores. In other words, the $C_3$ is not residing in a hot core. The abundances of the additional species chemically related to $C_3$, which we consider for the case of DR21(OH), provided further insight regarding the envelope conditions.

Table 6 summarizes the observed abundances of the different species in DR21(OH) as well as those available in the literature for two types of sources: the lukewarm corinos L1527 and B228 and the hot corino IRAS 16293-2422. We find that while $C_3$ has not been observed in any of the other sources, the abundances of the other three species in DR21(OH) are closer to the abundances observed in lukewarm corinos. In addition, the chemical model that best represents the observed abundances corresponds to a $T_{max}$ of 30–50 K, a temperature that is much lower than the values expected in hot cores/corinos. This suggests that the envelope of DR21(OH) is chemically closer to a WCCC region such as a lukewarm corino envelope than to a hot core. Furthermore, the predepletion $C_3$ abundance (at $t \leq 10^4$ yr) exceeds the observed values by a large factor. This implies that the $C_3$ abundance is primarily maintained via ion-molecule chemistry in the gas phase after $CH_4$ is desorbed from the surface of the dust grains and does not have a one-to-one correlation with $C_2$ as found in diffuse clouds.

### 5.4. Chemical and dynamical ages of the region

The chemistry of the envelope surrounding the embedded sources MM1 and MM2 in DR21(OH) appears to have occurred over a period between (0.7–3) Myr, including a cold period, warm-up, and extended time at $T$ = 30 or 50 K. This time period seems to be on the longer side of the evolutionary timescales of massive star-forming cores. As detailed by Csengeri et al. (2011), the lifetime of the gas in massive dense cores is determined by the crossing times or the local free-fall times for the molecular dense cores which is $(5–7) \times 10^4$ yr. However, the large-scale flows associated with Cygnus X (and DR21 in particular) are massive enough to continuously replenish the mass of these cores, allowing them to remain "active" for a much longer period of time. In addition, the dynamical time of the most massive sub-filament in DR21 is $\sim 2$ Myr (Schneider et al. 2010). Thus, the chemical age of $\sim 1$ Myr is consistent with the dynamical age of the region.

## 6. Summary

Using the high-velocity resolution of HIFI, in the DR21(OH) region, we detect absorption due to $C_3$ from the envelope and the less evolved core (MM2) as well as a rather weak signal associated to the most massive and hottest region (MM1). The abundance of $C_3$ in the envelope of the hot core associated with DR21(OH) has been consistently explained along with those of other species formed in the same chemical network using a chemical model involving the warm-up of grains. The formation mechanism of $C_3$ required to explain the observed abundances in dense star-forming regions is the gas-phase reaction of $CH_4$ desorbed from the grain surfaces that have been warmed up. It is neither formed in a cycle with $C_2$ as the starting point nor produced by the photodestruction cascades of PAH molecules. For the envelope of DR21(OH), the chemical models that best explain the abundances of $C_3$ and other chemically related species correspond to models 2 and 3, $n_{H_2}$ = $1$–$5 \times 10^6$ cm$^{-3}$ for $T_{max}$ = 30 K, for a time period between 0.7–3 Myr and model 6, $n_{H_2}$ = $5 \times 10^6$ cm$^{-3}$ for $T_{max}$ = 50 K, for a time period between 0.6–0.8 Myr. The upper limit of the timescale, though much larger than the typical lifetimes of hot (warm) cores, is not unrealistic in the case of DR21(OH), where the dynamic age of the most massive filament has been estimated to be 2 Myr.

## References

Ádámkovics, M., Blake, G. A., & McCall, B. J. 2003, ApJ, 595, 235
Aikawa, Y., Wakelam, V., Garrod, R. T., & Herbst, E. 2008, ApJ, 674, 984
Araya, E. D., Kurtz, S., Hofner, P., & Linz, H. 2009, ApJ, 698, 1321
Argon, A. L., Reid, M. J., & Menten, K. M. 2000, ApJS, 129, 159
Bernst, I., Schilke, P., Moeller, T., et al. 2011, Astronomical Data Analysis Software and Systems XX, 442, 505
Beuther, H., Semenov, D., Henning, T., & Linz, H. 2008, ApJ, 675, L33
Bisschop, S. E., Jørgensen, J. K., van Dishoeck, E. F., & de Wachter, E. B. M. 2007, A&A, 465, 913
Cazaux, S., Tielens, A. G. G. M., Ceccarelli, C., et al. 2003, ApJ, 593, L51
Cernicharo, J., Goicoechea, J. R., & Caux, E. 2000, ApJ, 534, L199
Chandler, C. J., Moore, T. J. T., Mountain, C. M., & Yamashita, T. 1993, MNRAS, 261, 694
Comito, C., Schilke, P., Phillips, T. G., et al. 2005, ApJS, 156, 127
Csengeri, T., Bontemps, S., Schneider, N., et al. 2011, ApJ, 740, L5
Fish, V. L., Reid, M. J., Argon, A. L., & Zheng, X.-W. 2005, ApJS, 160, 220
de Graauw, T., Helmich, F. P., Phillips, T. G., et al. 2010, A&A, 518, L6
Galazutdinov, G., Pętlewski, A., Musaev, F., et al. 2002, A&A, 395, 969

Garrod, R. T., & Herbst, E. 2006, A&A, 457, 927

Garrod, R. T., Wakelam, V., & Herbst, E. 2007, A&A, 467, 1103

Gendriesch, R., Pehl, T. F., Winnewisser, G., et al. 2003, Z. Naturforsch., 58a, 129

Gerin, M., De Luca, M., Black, J., et al. 2010, A&A, 518, L110

Gerin, M., Kaźmierczak, M., Jastrzebska, M., et al. 2011, A&A, 525, A116

Giesen, T. F., Van Orden, A. O., Cruzan, J. D., et al. 2001, ApJ, 551, L181

Haffner, L. M., & Meyer, D. M. 1995, ApJ, 453, 450

Hasegawa, T. I., Herbst, E., & Leung, C. M. 1992, ApJS, 82, 167

Hassel, G. E., Herbst, E., & Garrod, R. T. 2008, ApJ, 681, 1385

Hassel, G. E., Harada, N., & Herbst, E. 2011, ApJ, 743, 182

Hinkle, K. W., Keady, J. J., & Bernath, P. F. 1988, Science, 241, 1319

Maier, J. P., Lakin, N. M., Walker, G. A. H., et al. 2001, ApJ, 553, 267

Mangum, J. G., Wootten, A., & Mundy, L. G. 1991, ApJ, 378, 576

Mangum, J. G., Wootten, A., & Mundy, L. G. 1992, ApJ, 388, 467

Mauersberger, R., Henkel, C., Wilson, T. L., & Walmsley, C. M. 1986, A&A, 162, 199

Mookerjea, B., Giesen, T., Stutzki, J., et al. 2010, A&A, 521, L13

Motte, F., Bontemps, S., Schilke, P., et al. 2007, A&A, 476, 1243

Müller, H. S. P., Schlöder, F., Stutzki, J., & Winnewisser, G. 2005, J. Mol. Struct., 742, 215

Öberg, K. I., Fuchs, G. W., Awad, Z., et al. 2007, ApJ, 662, L23

Öberg, K. I., Linnartz, H., Visser, R., & van Dishoeck, E. F. 2009a, ApJ, 693, 1209

Öberg, K. I., van Dishoeck, E. F., & Linnartz, H. 2009b, A&A, 496, 281

Oka, T., Thorburn, J. A., McCall, B. J., et al. 2003, ApJ, 582, 823

Ott S. 2010, in Astronomical Data analysis Software and Systems XIX, eds. Y. Mizumoto, K. I. Morita, & M. Ohishi, ASP Conf. Ser., in press

Pety, J., Teyssier, D., Fossé, D., et al. 2005, A&A, 435, 885

Pilbratt, G. L., Riedinger, J. R., Passvogel, T., et al. 2010, A&A, 518, L1

Pineau des Forêts, G., Flower, D. R., & Dalgarno, A. 1988, MNRAS, 235, 621

Plambeck, R. L., & Menten, K. M. 1990, ApJ, 364, 555

Radi, P. P., Bunn, T. L., Kemper, P. R., Molchan, M. E., & Bowers, M. T. 1988, J. Chem. Phys., 88, 2809

Reipurth, B., & Schneider, N. 2008, Handbook of Star Forming Regions, Vol. I, 36

Richardson, K. J., Sandell, G., Cunningham, C. T., & Davies, S. R. 1994, A&A, 286, 555

Roelfsema, P. R., Helmich, F. P., Teyssier, D., et al. 2012, A&A, 537, A17

Roueff, E., Felenbok, P., Black, J. H., & Gry, C. 2002, A&A, 384, 629

Rygl, K. L. J., Brunthaler, A., Sanna, A., et al. 2012, A&A, 539, A79

Sakai, N., Sakai, T., Hirota, T., & Yamamoto, S. 2008, ApJ, 672, 371

Sakai, N., Sakai, T., Hirota, T., Burton, M., & Yamamoto, S. 2009a, ApJ, 697, 769

Sakai, N., Sakai, T., Hirota, T., & Yamamoto, S. 2009b, ApJ, 702, 1025

Schilke, P., Phillips, T. G., & Mehringer, D. M. 1999, The Physics and Chemistry of the Interstellar Medium, 330

Schmuttenmaer, C. A., Cohen, R. C., Pugliano, N., Heath, J. R., & Cooksy, A. L. 1990, Science, 249, 897

Schneider, N., Csengeri, T., Bontemps, S., et al. 2010, A&A, 520, A49

Van Orden, A., Cruzan, J. D., Provencal, R. A., et al. 1995, in Proc. Airborne Astronomy Symp. on the Galactic Ecosystem, eds. M. R. Haas, J. A. Davidson, & E. F. Erickson (San Francisco: ASP), ASP Conf. Ser., 73, 67

White, G. J., Abergel, A., Spencer, L., et al. 2010, A&A, 518, L114

Wilson, T. L., & Mauersberger, R. 1990, A&A, 239, 305

Zapata, L. A., Loinard, L., Su, Y.-N., et al. 2012, ApJ, 744, 86